Computational Prediction of the Effect of Microcavitation on an Atomization Mechanism in a Gasoline Injector Nozzle

Jun Ishimoto[1]
Institute of Fluid Science,
Tohoku University,
Sendai 980-8577, Japan
e-mail: ishimoto@alba.ifs.tohoku.ac.jp

Fuminori Sato

Gaku Sato

KEIHIN Co.,
Tochigi R&D Center,
2021-8 Hoshakuji, Takanezawa-machi,
Shioya-Gun,
Tochigi 329-1233, Japan

The effect of microcavitation on the 3D structure of the liquid atomization process in a gasoline injector nozzle was numerically investigated and visualized by a new integrated computational fluid dynamics (CFD) technique for application in the automobile industry. The present CFD analysis focused on the primary breakup phenomenon of liquid atomization which is closely related to microcavitation, the consecutive formation of liquid film, and the generation of droplets by a lateral flow in the outlet section of the nozzle. Governing equations for a high-speed lateral atomizing injector nozzle flow taking into account the microcavitation generation based on the barotropic large eddy simulation-volume of fluid model in conjunction with the continuum surface force model were developed, and then an integrated parallel computation was performed to clarify the detailed atomization process coincident with the microcavitation of a high-speed nozzle flow. Furthermore, data on such factors as the volume fraction of microcavities, atomization length, liquid core shapes, droplet-size distribution, spray angle, and droplet velocity profiles, which are difficult to confirm by experiment, were acquired. According to the present analysis, the atomization rate and the droplets-gas atomizing flow characteristics were found to be controlled by the generation of microcavitation coincident with the primary breakup caused by the turbulence perturbation upstream of the injector nozzle, hydrodynamic instabilities at the gas-liquid interface, and shear stresses between the liquid core and periphery of the jet. Furthermore, it was found that the energy of vorticity close to the gas-liquid interface was converted to energy for microcavity generation or droplet atomization. [DOI: 10.1115/1.4000264]

1 Introduction

Regarding the primary breakup process of fuel in an internal combustion (IC) engine, the effect of cavitation generated upstream of the nozzle aperture is known to be a very important factor in the determination of the atomization behavior of fuel injection, an essential factor in the operation and performance of such engines. Especially with regard to the cavitation in the injector nozzle, the magnitude of cavity generation, growth, and collapse in the sequential process is characteristically quite small and localized. The cavity shape is transformed on the order of 10–80 μm, this phenomenon being quite different from that of conventional hydrofoil cavitation. Thus, such cavitation behavior is termed "microcavitation." Microcavitation can be thought of as slight vaporization induced by a flow-generated local pressure drop. High-pressure fuel injectors, in which microcavitation frequently occurs, are used in both diesel and direct gasoline injection (DGI) engines whose manufacturability is closely related to the automobile industries. For IC engines (both gasoline and diesel), control of exhaust emission (such as unburned hydrocarbons and NO_x) and engine efficiency depends directly on atomization with microcavitation of the liquid jet inside the combustion chamber (direct injection) or inside the admission pipe (indirect injection). However, in recent studies on the atomization mechanism in injector nozzles, no significant results on the effect of microcavitation generation in the upstream condition on the liquid breakup phenomena have been obtained. The reason for the difficulties in clarifying such effects is that the visualization of microcavitation in an atomizing injector nozzle flow by optical experiments is very difficult because the microcavitation is frequently generated in a limited small region of several dozen micrometers downstream or upstream from the nozzle aperture. This extremely small region is invisible because the aperture is covered by an opaque metal jacket. With optical measurement using a high-speed camera, only the large region downstream of the aperture can be visualized. Furthermore, visualization is difficult because the microcavity is quite small, and also because the cyclic phenomena of microcavity generation and dissipation occur within a very short time. To overcome such experimental difficulties, results of integrated computational fluid dynamics (CFD) analysis combined with measurement data are a useful tool to test many configurations in a short time, enabling prediction of the location of microcavity generation in different types of injectors with various operational parameters, such as injector positions, injection timing, duration, etc. Fundamental research on atomization and multiphase processes, including the effect of microcavity generation in the injector nozzle, is multidisciplinary in the sense that it involves the disciplines of fluid mechanics, multiphase systems, measurement techniques, and modeling [1–3]. Around the portion of the microcavity, the region of vapor is a small continuous bubbly cloud. Therefore, microcavitation in high-speed flow as in gasoline injectors is almost isothermal, but compressibility effects may be important, particularly if the cavitation is unstable and vapor bubbles enter the liquid core and collapse causing pressure waves to interfere/enhance the liquid jet. The primary breakup mechanism of microcavitation generation controls both the length and the evolution of the potential core region (liquid core region where the magnitude of velocity is not damped toward the central axis) of the spray as well as generating all the characteristics of

[1]Corresponding author.

Contributed by the IC Engine Division of ASME for publication in the JOURNAL OF ENGINEERING FOR GAS TURBINES AND POWER. Manuscript received February 24, 2009; final manuscript received August 24, 2009; published online May 20, 2010. Assoc. Editor: Christopher Rutland.

the dispersed region (droplet size, spray angle, etc.) [4–8]. The rate of primary atomization with microcavitation controls the mass fraction of the perturbed liquid fragments ejected from the core region. To date, only a few CFD studies on nozzle jet flow with cavitation have been performed, the main results of those studies being as follows: A numerical model that treats liquid and vapor as a continuum has been constructed for predicting small-scale, high-speed, cavitating, nozzle flow by Schmidt et al. [9]. The coupled standard discrete droplet model, conventional breakup model, and Eulerian multifluid model have been applied to analyze cavitating nozzle flow by von Berg et al. [10]. Two-dimensional simulation of the strong interaction of cavitating nozzle flow with the outside jet formation has been performed and the direct interaction between the cavitation and the jet has been analyzed by Yuan and Schnerr [11]. However, those studies did not sufficiently focus on the turbulent primary breakup phenomena, and the conventional numerical model they employed does not have a sufficiently high resolution to analyze the primary breakup phenomena of microcavitation generation. As their models do not include accurate turbulence modeling such as large eddy simulation (LES), they are limited to the analysis of micro-scale turbulent atomization and cavitation phenomena.

The present integrated CFD analysis focused on the detailed behavior of the microcavitation generation of turbulent atomizing flow in a gasoline injector nozzle. The computation was performed for the primary breakup phenomena of liquid atomization, including that in the region upstream of the aperture, which is closely related to microcavitation generation, the consecutive formation of liquid film, and generation of droplets of a lateral high-speed turbulent flow in the outlet section of the nozzle. It is also possible to accurately simulate microscale complex two-phase atomizing flow with primary break-up, coalescence, compressibility effects, and even the interaction between unstable cavitation and the free surface. Governing equations for high-speed lateral atomizing injector nozzle flow taking into account the microcavitation generation based on the barotropic large eddy simulation-volume of fluid (LES-VOF) model in conjunction with the continuum surface force (CSF) model were developed. Then an integrated massively parallel computation was performed to clarify the detailed atomization process coincident with the microcavitation of a turbulent nozzle flow.

2 Governing Equations for Continuum-Barotropic Models of Cavitation

The basis of the continuum-barotropic approach to cavitation is a compressible mixture form of continuity and momentum equations. In this system, the mixture density is obtained by the following equation:

$$\rho = \alpha\rho_{lv} + (1-\alpha)\rho_g \tag{1}$$

where α is the liquid-vapor mixture phase volume fraction, ρ_g is the gas-phase density, and ρ_{lv} is the liquid-vapor mixture density which is given by Eq. (8), which will be appear in Sec. 2.1. The present model comprises a single set of conservation equations for the whole flow field, even though fluid properties are discontinuous across the fluid boundaries. These equations are written as follows.

The mass conservation equation is

$$\frac{\partial\rho}{\partial t} + \nabla\cdot(\rho\boldsymbol{v}) = 0 \tag{2}$$

and the momentum equation is

Table 1 Numerical conditions

Nozzle aperture diameter	d	2.26×10^{-4}	m
Liquid-phase density	ρ_l	732.0	kg/m^3
Gas-phase density	ρ_g	1.134	kg/m^3
Inlet pressure	$p_{l(\mathrm{in})}$	0.444	MPa
Outlet pressure	$p_{l(\mathrm{ex})}$	0.101	MPa
Liquid-phase dynamic viscosity	μ_l	4.42×10^{-4}	Pa s
Gas-phase dynamic viscosity	μ_g	1.51×10^{-5}	Pa s
Surface tension	σ_l	0.0198	N/m
Compressibility of vapor phase	ψ_v	4.62×10^{-5}	
Compressibility of liquid phase	ψ_l	8.37×10^{-7}	
Compressibility of gas phase	ψ_g	1.13×10^{-5}	
Reynolds number	Re	4.49×10^{3}	
Weber number	We	1.20×10^{3}	
Ohnesorge number	Oh	7.72×10^{-3}	

$$\frac{\partial}{\partial t}(\rho\boldsymbol{v}) + \nabla\cdot(\rho\boldsymbol{v}\boldsymbol{v}) = -\nabla p + \nabla\cdot\boldsymbol{\tau} + \int_{S(t)}\sigma\kappa'\boldsymbol{n}'\delta(\boldsymbol{x}-\boldsymbol{x}')dS \tag{3}$$

where $\boldsymbol{n}$ represents a unit vector normal to the liquid surface. The last term on the right-hand side of Eq. (3) represents the source of momentum due to surface tension. It acts only at the interface (represented by the Dirac function $\delta(\boldsymbol{x})$) over the entire surface described by $S(t)$.

The cavitation process is treated as an isothermal process using an equilibrium barotropic equation of state and the homogeneous equilibrium model (HEM) assumption [9], in which the effective compressibility of the liquid-vapor "mixture" is obtained from a model for the speed of sound in the "mixture." The most common barotropic model used for cavitation is based on the equilibrium equation, which is derived as follows:

$$\frac{\mathrm{D}\rho}{\mathrm{D}t} = \frac{1}{a^2}\frac{\mathrm{D}p}{\mathrm{D}t} \tag{4}$$

where a is the velocity of pressure waves (the sound velocity) in the cavitating mixture. This equation can be integrated analytically between liquid and vapor states as in the work of Schmidt [9] to obtain an equation of state in standard form, but this leads to a potential inconsistency between the mixture and liquid-vapor equations of state. Alternatively, Eq. (4) can be used directly with mixture continuity equation (2) to formulate a pressure equation. A pressure equation is formulated from the momentum equation and mixture continuity, including the phase compressibility terms implicitly. Following the pressure solution, the velocity, phase fraction, and mixture densities are corrected. This approach has proved to be problematic because the nonequilibrium nature of the closure means that the mixture pressure and density are not consistent with liquid or vapor equations of state until equilibrium is attained, and even then, numerical errors may accumulate, resulting in inconsistencies even at equilibrium. To avoid these difficulties, a new equilibrium barotropic model is proposed in which the pressure and density are guaranteed to obey the liquid and vapor equations of state until the limits and the equations of a mixture compressibility model. All three phases are considered to be compressible with the densities ρ_l (liquid), ρ_g (gas), and ρ_v (vapor) obtained from the pressure p and the phase compressibilities ψ_l, ψ_g, and ψ_v, respectively. The phase compressibilities are given as constant values as listed in Table 1. Simple linear models for the vapor and liquid equations of state are introduced as follows:

$$\rho_v = \psi_v p \tag{5}$$

$$\rho_l = \rho_l^0 + \psi_l p \tag{6}$$

The cavitation vapor-phase fraction obtained from the mixture density and the saturation conditions is introduced as follows:

$$\gamma = \max\left[\min\left(\frac{\rho_l^{\text{sat}} - \rho_{lv}}{\rho_l^{\text{sat}} - \rho_v^{\text{sat}}}, 1\right), 0\right] \tag{7}$$

namely, γ means the volume fraction of vapor in the liquid-vapor cavitating mixture. If the mixture density is obtained from the equilibrium equation of state, then

$$\rho_{lv} = (1-\gamma)\rho_l^0 + [\gamma\psi_v + (1-\gamma)\psi_l]p^{\text{sat}} + \psi(\gamma)(p - p^{\text{sat}}) \tag{8}$$

where $\psi(\gamma)$ is the mixture compressibility. Then when the limit of γ approaches 1, the mixture density ρ_{lv} will obey Eq. (5), provided that $\psi(\gamma) \to \psi_v$, and in the limit $\gamma \to 0$, the mixture density ρ_{lv} will obey Eq. (6), provided that $\psi(\gamma) \to \psi_l$. In this formulation, the model for mixture compressibility can be chosen to represent the particular form of the cavitation region. For example, the simple linear model of the liquid-vapor mixture phase compressibility $\psi(\gamma)$ for continuous cavitation is expressed as follows:

$$\psi(\gamma) = \gamma\psi_v + (1-\gamma)\psi_l \tag{9}$$

The above relationship would be appropriate and consistent with the way the interface is handled in the VOF approach. In bubbly cavitation, the sound velocity in the mixture of two-phase fluid is much lower than that of the single-phase fluid, and hence the apparent compressibility is much higher. Many models of sound velocity in a bubbly mixture have been employed in previous research, and the Wallis model is commonly used for cavitating flow [9], the isothermal assumption of which is employed in the following new model by which the liquid-vapor mixture phase compressibility $\psi(\gamma)$ is obtained,

$$\psi(\gamma) = [\gamma\rho_v^{\text{sat}} + (1-\gamma)\rho_l^{\text{sat}}]\left[\frac{\gamma\psi_v}{\rho_v^{\text{sat}}} + (1-\gamma)\frac{\psi_l}{\rho_l^{\text{sat}}}\right] \tag{10}$$

The advantages of this approach are as follows:

1. It is a fully compressible model.
2. The assumptions of Eqs. (8), (5), and (6) approximately satisfy the standard pressure equation which can be applied to subsonic flow.
3. The compressibility of the mixture is properly taken into account.

2.1 VOF Model With Cavitating Phase. The present cavitation model described in Sec. 2 can be included in the compressible VOF formulation to simulate systems including both a free surface and low-pressure vaporization. Namely, the present model takes into account the three liquid, gas, and vapor phases by treating the system as having two phases: cavitating liquid-vapor and gas. The disadvantage of this representation is not only that the gas and liquid are immiscible, but also that the gas and vapor are considered to be immiscible because the liquid and vapor are not logically separate phases but a cavitating mixture. In principle the gas-phase can appear when the γ of the cavitating flow condition is nonzero in the region, where $\alpha=0$; however, this is a probabilistic view, i.e., if liquid were present it would vaporize and the actual vapor-phase fraction in the system which represents the cavitation is in the form of $\alpha\gamma$. α is obtained by the multidimensional bounded explicit solution of the phase-fraction equation, including the compression term newly developed from interFoam and lesInterFoam [12]. Additionally, γ is not obtained by direct solution of a phase fraction equation but from the density of the liquid-vapor mixture ρ_{lv}, which is obtained at the prediction stage by the implicit solution of a transport equation and at the pressure correction stage from the corrected pressure. The gas-phase density ρ_g is similarly solved. If a linear model is also used for the gas phase, the following equation is introduced,

$$\rho_g = \psi_g p \tag{11}$$

The compressibilities of all three phases can be combined when formulating the pressure equation.

2.2 Basic Equations for Immiscible Fluids. The numerical model represents the simultaneous unsteady flow of two immiscible compressible fluids of the liquid-vapor phase and the gas-phase, each having a constant viscosity and including surface tension. The flow is considered to be a turbulent compressible Newtonian and isothermal flow governed by the Navier–Stokes equations and continuity equation as shown in Eqs. (3) and (2), respectively. The numerical simulation of atomizing flow composed of two immiscible fluids of the liquid-vapor phase and the gas-phase involves two coupled tasks: (1) resolving the flow field and (2) updating the position of the interface. The first task is completed by solving the Navier–Stokes equations taking into account the effect of the subgrid-scale atomizing flow field by LES [13,14]. The second task is performed using the VOF method [15–17], which actually maintains and updates the field of volume fraction of one fluid in each cell instead of the existence of the fluid at the surface location. The advantage of the VOF method is that there are no topological constraints. Thus, the VOF method has been widely used to track the interface of two immiscible fluids, such as water and air. The surface tension is taken into account through the CSF model [18], where the surface force is transformed to a body force which is only nonzero in the interface region of limited thickness. The scalar α is used to denote the volume fraction field, also called the VOF field [15–17]. Therefore, the governing equations for the one-fluid VOF-CSF model include the Navier–Stokes equations, continuity equation, and VOF advection equation. When the interface is advected by the flow, the evolution of the VOF advection function is given by

$$\frac{\partial\alpha}{\partial t} + \nabla\cdot(\alpha\boldsymbol{v}) = 0 \tag{12}$$

The interface between the phases is simultaneously computed using a surface capturing methodology which employs the volume fraction of one of the phases (here taken to be the liquid-vapor phase) as an indicator function α to identify the different fluids. The interface is not defined as a sharp boundary, and a transition region exists where the fluid is treated as a mixture of the two fluids on each side of the interface, which would in reality be a discontinuous step. The indicator function, which is equivalent to the liquid-vapor phase volume fraction α, is defined as

$$\alpha = \begin{cases} 0 & \text{for a cell inside the gas-phase} \\ 0 < \alpha < 1 & \text{for a cell in the transitional region} \\ 1 & \text{for a cell completely in the liquid-vapor phase} \end{cases}$$

The VOF advection in Eq. (12) appears in the conservative form adopted from Puckett et al. [17]. According to the definition of the indicator function α, the local density ρ and the local viscosity μ of the fluid are typically interpolated across the interface as follows:

$$\begin{cases} \rho = \alpha\rho_{lv} + (1-\alpha)\rho_g \\ \mu = \alpha\mu_{lv} + (1-\alpha)\mu_g \end{cases} \tag{13}$$

Since the interface is treated as a transitional zone, its exact shape and location are not explicitly known. During the numerical solution process, the free-surface boundary conditions are applied. There are three hydrodynamic boundary conditions at the free surface: normal stress balance, tangential stress balance, and the kinematic equation. The kinematic condition is implied by the VOF advection. The surface integral in Eq. (3) that represents the surface tension, therefore, cannot be calculated directly. Brackbill et al. [18] overcame this problem with their CSF model, which represents the surface tension effects as a continuous volumetric force acting within the transition region.

The stress balance of dynamics is realized through the CSF model incorporated in the momentum equations by introducing a body force $\boldsymbol{F}_{sv}$. The surface tension can be modeled numerically

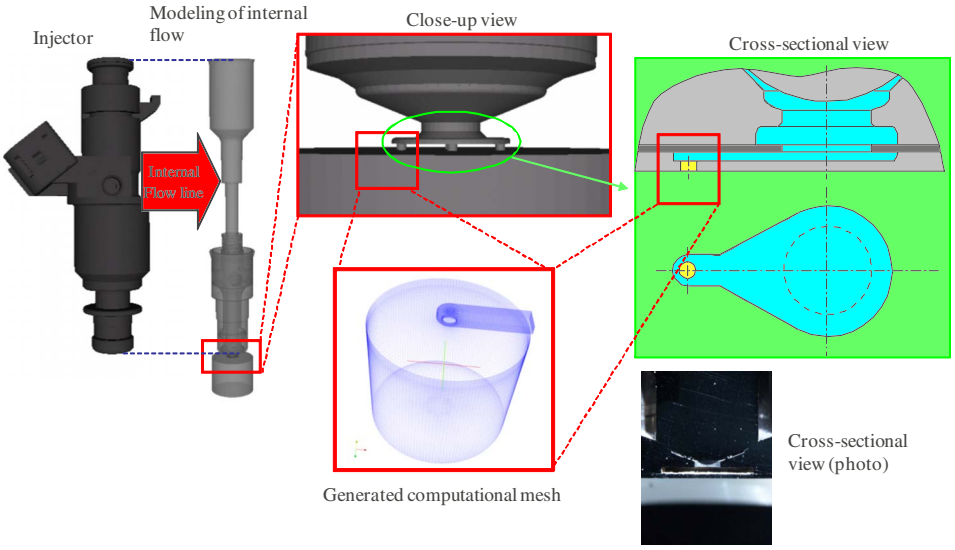

(*a*) Creation of computational domain and rectangular structured mesh based on the CAD data of actual gasoline injector nozzle

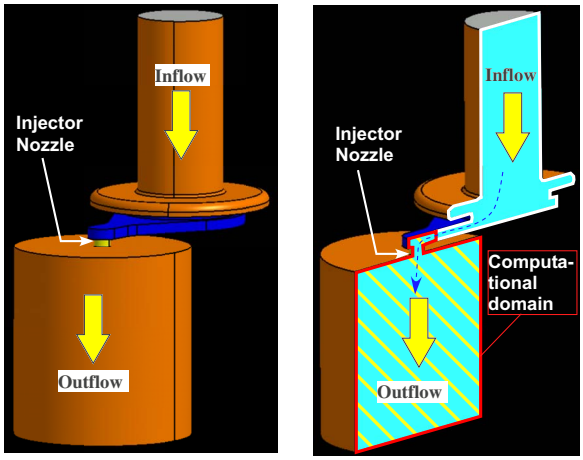

(*b*) Schematic of the internal lateral flow of gasoline injector nozzle

Fig. 1 Overview of the computational system employed by the present calculation

as a body force $\boldsymbol{F}_{sv}$ concentrated at the interface. The localized body force $\boldsymbol{F}_{sv}$ near the interface is calculated from the volume fraction data and is given by

$$\boldsymbol{F}_{sv} = \int_{s(t)} \sigma\kappa' \boldsymbol{n}' \delta(\boldsymbol{x} - \boldsymbol{x}') dS \approx \sigma\kappa \nabla \alpha \tag{14}$$

The characteristic interface parameters, the unit vector normal to the interface $\boldsymbol{n}$, and curvature κ are calculated as

$$\boldsymbol{n} = -\nabla\alpha, \quad \hat{\boldsymbol{n}} = \frac{\boldsymbol{n}}{|\boldsymbol{n}|} \tag{15}$$

$$\kappa = \nabla \cdot \hat{\boldsymbol{n}} \tag{16}$$

The body force term of $\boldsymbol{F}_{sv}$ in r.h.s. in momentum Eq. (3) effectively removes the explicit boundary condition at the interface in the governing equations. The LES-VOF equations are derived from Eq. (3) through a localized volume averaging of the phase weighted properties. This process is more commonly known as filtering because it removes the very small scales of motion from direct calculation. This averaging in conjunction with the nonlinear convection term in Eq. (3) produces an additional quantity into the momentum equation that cannot be directly calculated.

The effect of the subgrid scale on the resolved eddies in momentum Eq. (3) is represented by the SGS (subgrid-scale) stress, since it represents the effect of the unresolved small scale of turbulence. It is given by

The SGS stress is approximated by a single subgrid-scale model of the eddy viscosity type that can be written as

$$\boldsymbol{\tau}^{\mathrm{SGS}} - \frac{2}{3}k\boldsymbol{I} = -\frac{\mu^{\mathrm{SGS}}}{\rho}(\nabla\overline{\boldsymbol{v}} + \nabla\overline{\boldsymbol{v}}^T) \tag{18}$$

where k is the subgrid-scale turbulent energy and μ^{SGS} is the subgrid-scale viscosity, both of which are calculated by the one-equation SGS turbulent energy transport model:

$$\frac{\partial k}{\partial t} + \nabla \cdot (k\bar{\boldsymbol{v}}) = \nabla \cdot [(\nu + \nu^{\mathrm{SGS}}) \nabla k + \boldsymbol{\tau}^{\mathrm{SGS}} \cdot \bar{\boldsymbol{v}}]$$

$$- \epsilon - \frac{1}{2}\boldsymbol{\tau}^{\mathrm{SGS}} : (\nabla \bar{\boldsymbol{v}} + \nabla \bar{\boldsymbol{v}}^T) \tag{19}$$

$$\begin{cases} \epsilon = C_\epsilon k^{3/2}/\Delta \\ \nu^{\mathrm{SGS}} = C_k k^{1/2}/\Delta \end{cases} \tag{20}$$

where (ϵ) is the SGS turbulent dissipation and Δ is the SGS length scale corresponding to the filter width (in most cases equivalent to the cell size). The filter width Δ is defined as $\Delta = (\Delta_x \Delta_y \Delta_z)^{1/3}$, where Δ_x, Δ_y, Δ_z are the grid spacings in the x, y, and z directions, respectively. The constants, found from statistical considerations, are (C_k=0.07) and (C_ϵ=1.05). Additional "subgrid" terms are produced by the filtering of the integral in Eq. (3) and the convection term in Eq. (12). The former represents the subgrid-scale influence of surface tension, known as capillary force, and becomes important relative to the resolved surface tension when the surface curvature approaches the grid size. In cases where the influence of surface tension is small compared with that of inertia, the effect of subgrid-scale surface tension also becomes small. The latter term represents deformation of the liquid-gas interface due to subgrid-scale turbulence and is experienced at the grid scale as added interphase diffusion. This effect is in direct opposition to the estimated SGS surface tension force. Numerical effort has been made to preserve the sharpness of the gas-liquid interface. Both these SGS terms, which can be potentially used to construct a new model for closure, have not been developed to date. Taking this into account, in the present numerical condition of ($\mathrm{We} \gg 1$), the influence of surface tension was found to be relatively small compared with the effect of inertia at the resolved scales.

2.3 Computational Method. Figure 1 depicts an overview of the computational system employed by the present calculation. The computational domain and rectangular structured mesh are created with reference to the CAD data of actual injector nozzle geometry which are used in gasoline engines. The computational domain is available to precisely calculate the internal lateral flow of the injector nozzle. The geometry of the computational domain and the generated mesh are shown in Fig. 2. The generated mesh is sufficiently fine for application of the LES-VOF model. For the computational grid, the minimum mesh size around the nozzle inlet and outlet is 4.0 μm, and total number of mesh nodes is about 3.4 million. The lateral fluid flows into the outlet of the nozzle aperture and is dispersed in the extended free stream region with atomizing behavior. The extended free stream region is initially filled with air under atmospheric conditions. Namely, the fuel injection into the air is computed. The direction of the lateral inflow and the location of the nozzle aperture opening are geometrically orthogonal to each other. The nonslip condition for prescribed velocity is applied to the wall of the inflow section and nozzle throat section. A free-slip or freestream condition for the prescribed velocity is applied to the surrounding wall outlet domain of the nozzle throat.

The working fluid of the liquid phase is assumed to be gasoline and the gas-phase is assumed to be air at a pressure of 0.444 MPa, resulting in a liquid-gas density ratio of 645. The other numerical conditions are summarized in Table 1. Those numerical conditions are based on the visualization measurement condition in the present experiment. The initial numerical condition of inlet and outlet pressure, and flow rate are consistent with experimental conditions. Also, the nondimensional Reynolds, Mach, and Weber numbers clearly indicate that the injected flow is turbulent and subsonic and is in the so-called atomization regime, in which surface tension and viscous forces are likely only to be important at small scale. These conditions are in many respects reasonably

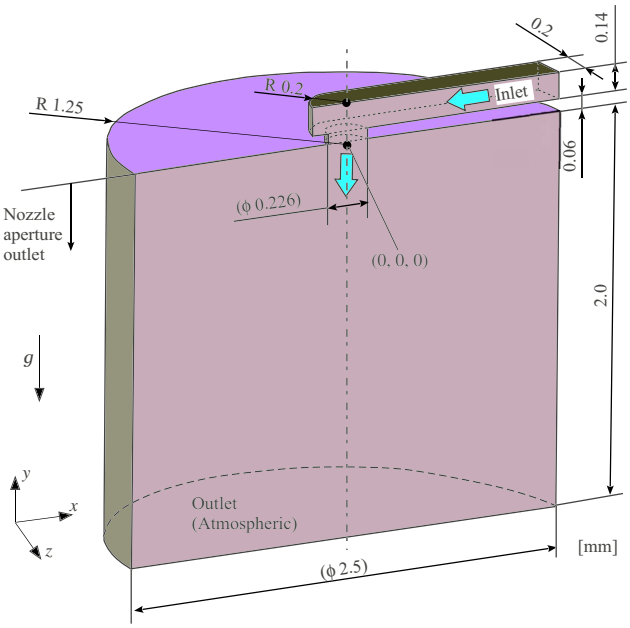

(*a*) Geometry of the computational domain

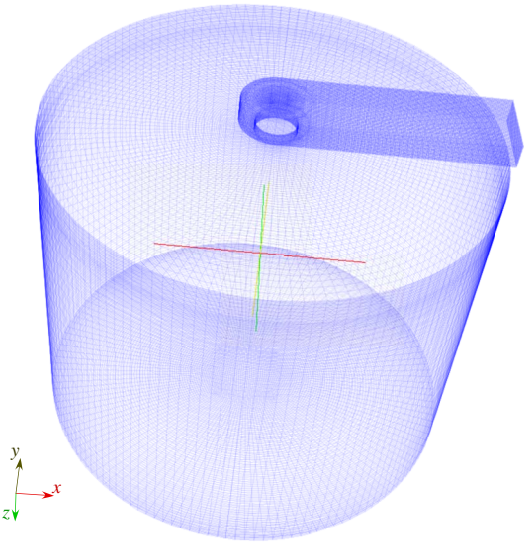

(*b*) Computational mesh employed

Fig. 2 Computational system for injector nozzle

representative of those in contemporary gasoline engines used in actual vehicles.

To compute the present system, we developed an original solver, named *cavitatingLesInterFoam*, using the OpenFOAM finite volume CFD open source code [19] based on the extended form of *interFoam* and *lesInterFoam* [12]. This new solver has a special feature that it can be used to calculate the atomizing flow, which accompanies cavitation phenomena. The conventional solver of *lesCavitatingFoam* in OpenFOAM version 1.5.x does not include the bounded interfacial breakup model. Namely, the conventional cavitation solver in OpenFOAM cannot compute accompanying atomization behaviors.

OpenFOAM employs spatial and temporal discretization schemes which are globally second-order accurate, but which preserve the proper limits on physically bounded variables. In the case of the convection term in the phase fraction transport Eq.

(12), this is achieved through a flux-limiting scheme and a conditional blending scheme where the solution might become unbounded. The newly developed solver of cavitatingLesInterFoam can compute a gas-liquid immiscible system in which the liquid phase can cavitate vapor introduced as a third-phase. The interface between the gas and the liquid is captured using a VOF-based approach with a compression term in the phase fraction equation rather than compressive differencing. The liquid-vapor interface does not require numerical compression as the physics of the cavitation process naturally maintains a sharp interface.

The interval of each time step is automatically adjusted during the computation to satisfy the Courant-Friedrichs-Lewy (CFL) condition. We actually calculated solutions on three different grid densities: 1.2 M, 3.4 M, and 5.4 M cell nodes. As a result, we found that each numerical result of volume fraction profile, velocity vector profile, and pressure distribution showed almost the same profile, and thus the grid density independence of the numerical results was confirmed. Therefore, as a compromise between computer memory and accuracy, we chose to use a 3.4 M structured grid for the calculations.

2.4 Numerical Schemes for Injection and Break-Up. The numerical procedure for phase fraction transport Eq. (12) is based on the CICSAM differencing scheme proposed by Ubbink and Issa [20]. Recently, Ubbink and Issa [20] proposed a compressive bounded high-resolution scheme, termed the compressive interface capturing scheme for arbitrary meshes (CICSAM) based on the normalized variable diagram (NVD) [21], to deal with contact discontinuities such as fluid interfaces.

CICSAM applies the NVD to ensure the boundness in approximating the face volume fluxes and switches between two different high-resolution schemes to ensure the sharpness of the interface. An overview of the CICSAM is given below to facilitate understanding of its theoretical background. The CISCAM scheme was formulated based on the idea of donor-acceptor formulation, i.e., as a scheme that varies as a function of the interface-cell face angle. The discretization depends on the direction of the interface velocity and the angle it makes with the integration cell face. However, rather than applying the downwind and upwind schemes as base schemes, it utilizes the Hyper-C scheme and ULTIMATE-QUICKEST (UQ) scheme of Leonard [21], the first being used when the cell face is directed perpendicular to the interface normal vector, and the latter being employed when the face normal vector is aligned with the normal to the interface.

The normalized variable of F forms the basis on which the high-resolution schemes are constructed and is defined as [21]

$$\hat{F} = \frac{F - F_U}{F_A - F_U} \tag{21}$$

where the subscript D denotes the donor cell, A denotes the acceptor cell, and U is the upwind cell. The upper bound of the convection boundness criterion (CBC) described in Eq. (22) is the most compressive differencing scheme because it converts all gentle gradients into sharp steps, as indicated by Leonard and termed Hyper-C [21].

$$\hat{F}_{f(\mathrm{CBC})} = \begin{cases} \min\left\{1, \dfrac{\hat{F}_D}{c}\right\} & \text{for } 0 \le \hat{F}_D \le 1 \\ \hat{F}_D & \text{for } \hat{F}_D < 0 \text{ or } \hat{F}_D > 1 \end{cases} \tag{22}$$

where c is the Courant number of the donor cell. Such a characteristic is desirable in the current modeling of moving interface problems. However, it is unstable due to its tendency to wrinkle the interface when the orientation of the interface is normal to the flow direction. To overcome this problem, the ULTIMATE-QUICKEST [21] described below is adopted in the CICSAM to continue the calculation where the Hyper-C is inadequate.

$$\hat{F}_{f(\mathrm{UQ})} = \begin{cases} \min\left\{\dfrac{8c\hat{F}_D + (1-c)(6\hat{F}_D + 3)}{8}, \hat{F}_{f\mathrm{CBC}}\right\} & \text{for } 0 \le \hat{F}_D \le 1 \\ \hat{F}_D & \text{for } \hat{F}_D < 0 \text{ or } \hat{F}_D > 1 \end{cases} \tag{23}$$

The UQ is a high-resolution differencing scheme, but it is still too diffusive to apply anywhere in the calculation of moving interface problems. Consequently, depending upon the orientation of the interface, a weighting factor $0 \ge \eta_f \ge 1$ is applied with CICSAM to enable smooth switching between these two methods:

$$\hat{F}_{f(\mathrm{CICSAM})} = \eta_f \hat{F}_{f(\mathrm{CBC})} + (1 - \eta_f)\hat{F}_{f(\mathrm{UQ})} \tag{24}$$

where η_l is related to the angle between the interface orientation and flow direction [20]. The fractional volume function on the cell face can then be obtained by rearranging Eq. (24) according to Eq. (21). Furthermore, the implicit pressure-implicit split-operator (PISO) algorithm in conjunction with conjugate gradient methods is employed in the solution procedure.

2.5 Phase Fraction Boundness in Compressible Flow. Maintaining phase-fraction boundedness in the numerical integration process is as important as in compressible flow. The phase fraction equations are obtained by the following equations:

$$\frac{\partial \alpha}{\partial t} + \boldsymbol{v} \cdot \nabla \alpha = -\alpha\beta\left(\frac{1}{\rho_{lv}}\frac{D\rho_{lv}}{Dt} - \frac{1}{\rho_g}\frac{D\rho_g}{Dt}\right) \tag{25}$$

$$\frac{\partial \beta}{\partial t} + \boldsymbol{v} \cdot \nabla \beta = -\alpha\beta\left(\frac{1}{\rho_g}\frac{D\rho_g}{Dt} - \frac{1}{\rho_{lv}}\frac{D\rho_{lv}}{Dt}\right) \tag{26}$$

where $\beta(=1-\alpha)$ is the gas-phase fraction. The transport is in bounded rather than conservative form, and the sources have an $\alpha\beta$ prefactor, which also ensures that boundedness is maintained providing that the terms are handled appropriately within the numerical scheme. This is achieved by evaluation:

$$C_\alpha = \left(\frac{1}{\rho_{lv}}\frac{D\rho_{lv}}{Dt} - \frac{1}{\rho_g}\frac{D\rho_g}{Dt}\right) \tag{27}$$

after and consistently with the discretization of the pressure equation and then choosing the way in which the term is handled implicitly according to the sign of this term. For example, in the solution of Eq. (25), if c_α was negative, the source term would be made implicit in α, which would ensure that $\alpha \ge 0$. However, if c_α was positive, it would be made implicit in β, in which case it would have features in both the diagonal and source of the matrix and ensure $\alpha \le 1$.

3 Results and Discussion

Figure 3 shows the instantaneous isocontour of the actual cavity fraction (vapor-phase fraction) $\alpha\gamma$ along with the liquid-vapor

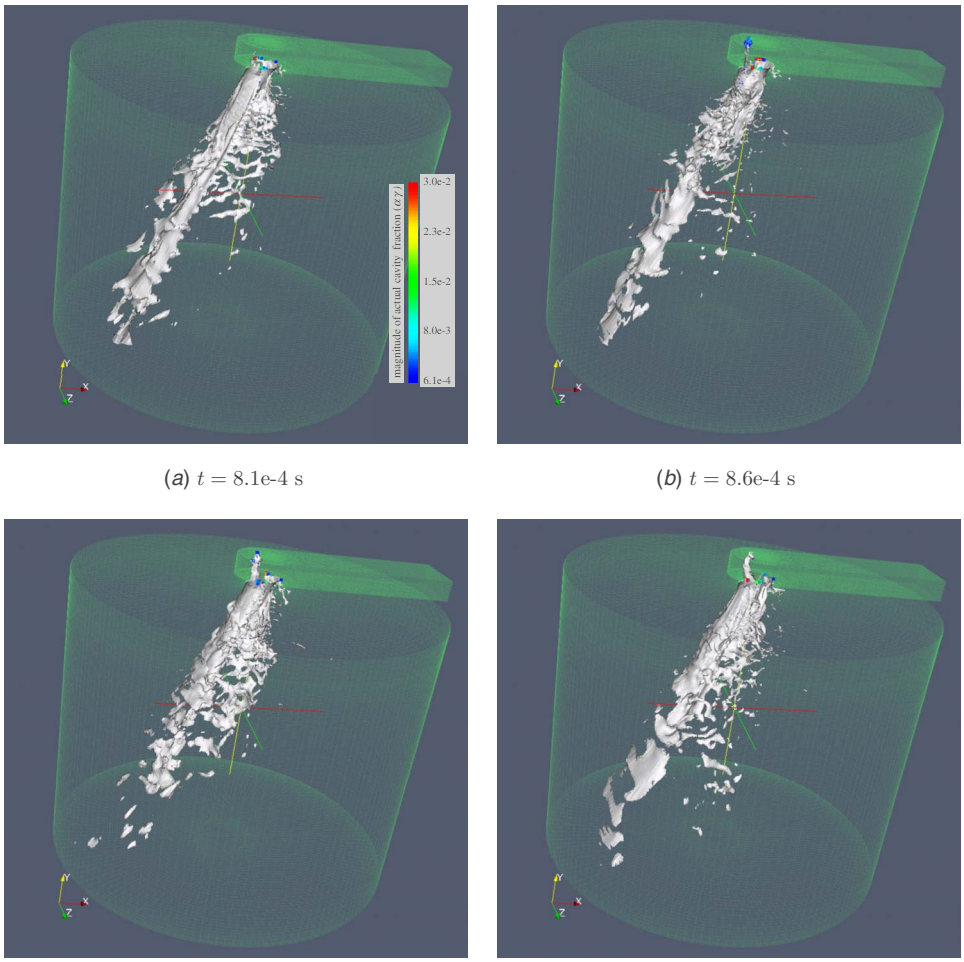

(*a*) $t = 8.1\text{e-}4$ s (*b*) $t = 8.6\text{e-}4$ s

(*c*) $t = 9.1\text{e-}4$ s (*d*) $t = 9.5\text{e-}4$ s

Fig. 3 Overview of the instantaneous isocontour of an actual cavity fraction (vapor-phase fraction) $\alpha\gamma$ along with the liquid-vapor phase volume fraction of α=0.5. The color graduation represents the scalar magnitude of cavity fraction $\alpha\gamma$.

phase volume fraction α. The threshold of the volume fraction is α=0.5 (gas-liquid interface). The color graduation represents the scalar magnitude of cavity fraction $\alpha\gamma$. Figure 5 shows the velocity vector profiles on the isosurface of α=0.5 just downstream of the nozzle aperture. Also, Fig. 6 shows the velocity vector profiles on the isocontour of $\alpha\gamma$, especially focused in the vicinity of the microcavity generated region.

With CFD analysis, it is possible to clearly elucidate the microcavitation behavior and atomization mechanism upstream of the nozzle aperture, which is invisible by visualization measurement. The microcavitation was found to be quite locally generated in the edge of the nozzle aperture and also generated in the portion where the curvature of the liquid-vapor phase fraction isosurface becomes large. As the vapor pressure of gasoline is relatively large, microcavities are easily generated in spite of the low velocity conditions. When the liquid film becomes thin due to stretching and the fluid velocity inside the thin liquid-film layer increases prior to turn-off, microcavitation is generated in that portion due to the local pressure drop. With time, a tornadolike small swirling flow is locally generated from the aperture toward the upstream region and microcavitation is actively generated there, especially around the center of the microvortex of the swirl. The magnitude of the microcavitation is mainly controlled by the degree of local pressure decrease closely related to the increase in scalar magnitude of the azimuthal component of liquid-phase velocity. Especially in the center of the small swirling vortex, as the magnitude of velocity becomes large, the vapor fraction of the cavity increases with a decrease in local static pressure.

As shown by Figs. 3–6, the hydrodynamic shear stress between the liquid core region and the liquid periphery region also becomes large because of an increase in the sharp velocity gradient in those regions. The combined effect of both those vortices initiates Kelvin–Helmholtz (K-H) instability at the interface. When the magnitude of the perturbation amplitude for liquid film is above a certain value due to turbulent generation resulting from the boundary layer separation at the nozzle throat, the liquid film in the nozzle downstream is stretched to form ligaments. The growth of most of the unstable waves is controlled by hydrodynamic shear stress with cavity generation, which results in the formation of liquid ligaments at the crest of each wave. Stretched by vortices in the gas phase, those ligaments break up into droplets.

Accordingly, the primary and sequential processes of the atomization mechanism with microcavitation generation in the injector nozzle, especially in the case of lateral fluid flow, orthogonal to vertical spraying flow is obtained by the present numerical method. Furthermore, stable high-resolution computation can be attained at the high density ratio of gas-liquid phase (ρ_l/ρ_g =645) conditions by using our numerical method. Compared with the visualization of spray behavior by an instantaneous high-speed

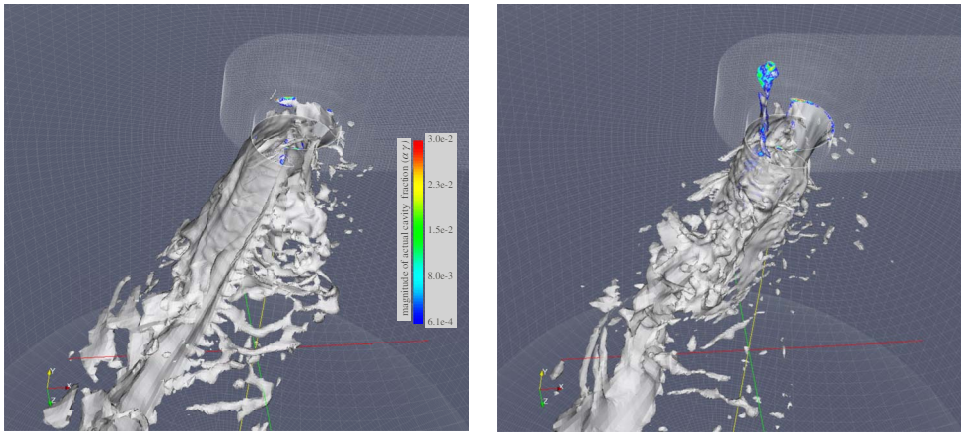

(*a*) $t = 8.1\text{e-}4$ s (Close-up view)

(*b*) $t = 8.6\text{e-}4$ s (Close-up view)

(*c*) $t = 9.1\text{e-}4$ s (Close-up view)

(*d*) $t = 9.5\text{e-}4$ s (Close-up view)

Fig. 4 Close-up view of the instantaneous isocontour of the actual cavity fraction (vapor-phase fraction) $\alpha\gamma$ along with the liquid-vapor phase volume fraction of α=0.5. The color graduation represents the scalar magnitude of cavity fraction $\alpha\gamma$.

photograph, which appears later in Fig. 9, the spray angle and the tendency of the breakup process reasonably agree with the numerical results.

Figure 7 shows the characteristics of the potential core of the liquid-phase jet flow just downstream of the nozzle aperture outlet. The potential core is represented by the superimposed results of the maximum liquid-vapor phase volume fraction (α=1) at all computational time steps (500 time steps). Namely, this figure is obtained by superimposing the calculation results of all time steps. The length of the potential core (breakup length; l_p) of the lateral atomizing nozzle flow is found to be shorter than that in the general axisymmetric nozzle flow such as that by previous analysis

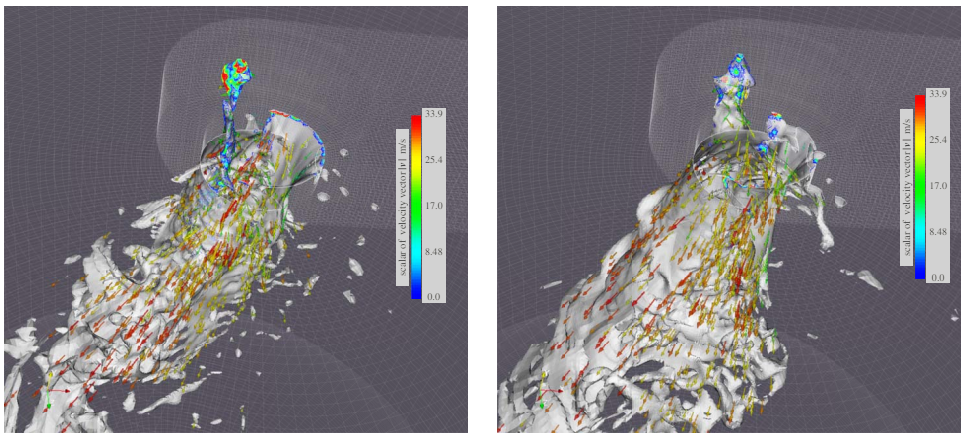

(*a*) $t = 8.6\text{e-}4$ s

(*b*) $t = 9.1\text{e-}4$ s

Fig. 5 Instantaneous velocity vector *v* profiles on the isosurface of α=0.5 just downstream of the nozzle aperture

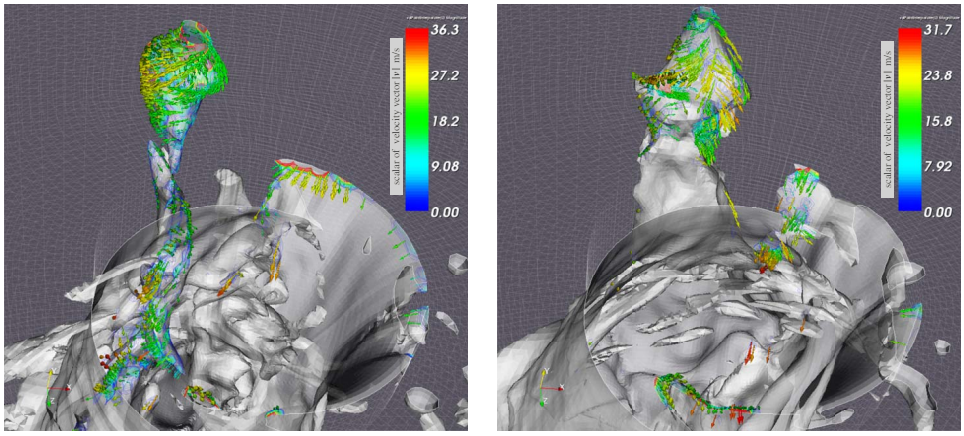

(*a*) $t = 8.6\text{e-}4$ s (*b*) $t = 9.1\text{e-}4$ s

Fig. 6 Instantaneous velocity vector *v* profiles on the isocontour of $\alpha\gamma$ around the vicinity of the cavity generated region

[4–7], namely, the present l_p approximately equals an aperture diameter d of $3d$ and $4d$ distance.

The short length of l_p is caused by the strong perturbation due to the change in direction of the parallel duct inflow to the orthogonal mainstream outflow at the aperture, and also due to the microcavity generation. Strong perturbation is induced by crimping the horizontal inflow at 90 deg in the direction of the vertical spray mainstream. Strong, rapid atomization is enhanced, especially in the vicinity of the microcavity generated-collapse region, and as a result, the potential core tends to be reduced, whereas the atomization length of the conventional axisymmetric nozzle flow generally tends to be larger. This numerically obtained spray angle characteristic agrees with that of the instantaneous photo image of injector spray experimentally obtained by high-speed camera, as later shown by Fig. 9.

Figures 8 and 9 show the characteristic atomizing spray behavior in comparison with the results with and without the cavitation model. The comparison was performed under the primary breakup of the initial unsteady condition, and the primary breakup of the quasisteady condition. Focusing on the effect of the microcavitation on primary breakup with atomization, computation without the cavitation model was conducted. By comparing the numerical results between the present cavitation model (Case (A)) and the one-fluid (without cavitation, nonvapor) model (Case (B)), such comparison was performed under two conditions: (1) an initial unsteady breakup condition and (2) a quasisteady breakup condition.

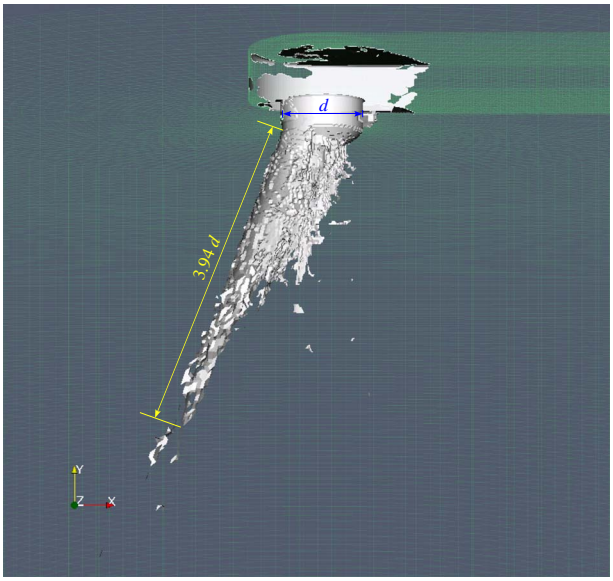

Fig. 7 Characteristics of the potential core of the lateral injector nozzle flow just downstream of the nozzle aperture outlet

In Case (A), as for microcavitation generation and its collapse, it was found that the minute perturbation around the gas-liquid boundary just downstream of the aperture vicinity is more effectively generated than in Case (B) because of the microcavitation generation and the collapse process. At the initial stage of the primary breakup process, due to liquid-phase flow acceleration which developed in the entrance duct connected to the orthogonal nozzle inlet aperture, and also due to the microcavity generation, large turbulent perturbations with separation flow were induced in the nozzle outlet section. The initial perturbations of the liquid column surface resulting from initial wave growth were due to a combination of microcavity generation, nozzle-generated turbulence, and relaxation of the velocity profile as the liquid exited from the aperture. However, as the effect of microcavity generation and the collapse mostly influences the occurrence of the minute perturbation around the gas-liquid boundary just downstream of the aperture, especially in the initial unsteady condition of the primary breakup process with large spray angle, the atomizing flow characteristics in Case (A) become stabler than those in Case (B) in the quasisteady condition.

From these results, it was confirmed that the microcavity generation influences the enhancement of the atomization of droplets, especially at the initial stage of the primary breakup process. After the conclusion of the initial stage of the primary breakup process, the effect of microcavity generation on the quasisteady breakup process becomes weak. Therefore, microcavitation plays a significant role as an enhancement factor of the initial unsteady breakup process, and also as a stabilization factor of the quasisteady breakup process. After those characteristic primary breakup phenomena, lateral inflow of a liquid column is transformed into a small wavy liquid film downstream of the aperture exit due to the small vortex induced by cavity generation and the wake passing through the nozzle throat, which is due to the effects of negative pressure gradient and nozzle generated turbulence. The continuous growth of the circumferential surface perturbations can be clearly seen.

By our experimental study on visualization measurement, the instantaneous photo images of actual injector spray phenomena

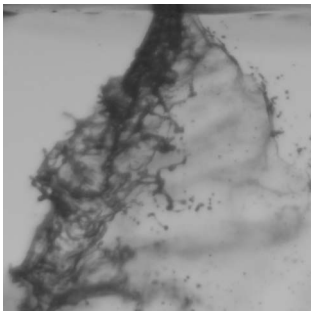

(*a*) Instantaneous photo image

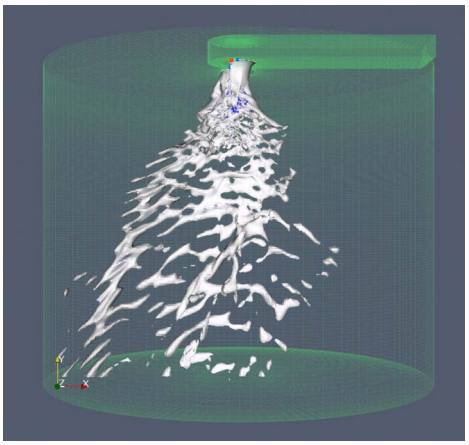

(*b*) Model with cavitation (Case (A))

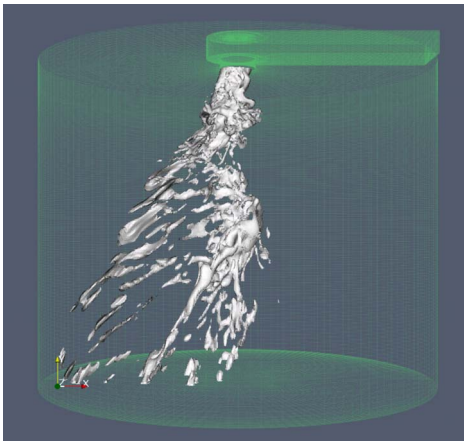

(*c*) Model without cavitation (Case (B))

Fig. 8 Characteristic atomizing spray behavior in comparison with results of models with and without cavitation under primary breakup at an initial unsteady condition ($t=4.1\times10^{-4}$ s)

captured by digital high-speed camera, as shown in Figs. 8 and 9, are compared with the numerical results of Case (A) and Case (B), respectively. It is ascertained that the model with cavitation (Case (A)) can more satisfactorily reproduce the spray cone aspect, the spray angle, the tendency of the breakup process, and the instability of the spray cone contour than Case (B). The numerically obtained value of the spray angle, $\theta_s=63.3$ deg, in the steady breakup condition reasonably agrees with the experimental result. Especially in the spray cone contour, the contour of the right side of the cone with an appropriate spray angle is successfully captured by the cavitation model (Case (A)). However, the dilute contour of the right side in the downstream direction could not be captured because the liquid-film thickness at the contour was quite thin. The present fine grid does not have sufficient resolution to capture such a thin liquid-film region. Furthermore, taking these results into account with the results shown in Figs. 3 and 4, the numerically obtained spray shape, the liquid-film breakup behavior, and the consecutive droplet atomization by the cavitation model reasonably agree with the experimental results. These results confirm the validity of the CFD analysis employed in this study and that CFD can be applied to actual design optimization of a gasoline injector nozzle.

To investigate the effect of vortex structure on turbulent atomization in the nozzle, the enstrophy E and the second invariant of velocity gradient tensor Q were calculated. Figures 10 and 11 show the isosurface of the enstrophy E and the second invariant of velocity gradient tensor Q profiles just inside and downstream of the nozzle, respectively. Figure 12 shows the isosurface of the second invariant of velocity gradient tensor Q profiles in the case without cavitation model. The color graduation in these figures represents the scalar magnitude of vorticity, $|\boldsymbol{\omega}|$. The second invariant Q is defined by the following equation:

$$Q=\frac{1}{2}(W_{ij}W_{ij}-S_{ij}S_{ij}) \tag{28}$$

where S_{ij} and W_{ij} denote the symmetric and antisymmetric parts of the velocity gradient tensor, respectively. These are defined as follows:

$$S_{ij}=\frac{1}{2}\left(\frac{\partial v_j}{\partial x_i}+\frac{\partial v_i}{\partial x_j}\right) \tag{29}$$

$$W_{ij}=\frac{1}{2}\left(\frac{\partial v_j}{\partial x_i}-\frac{\partial v_i}{\partial x_j}\right) \tag{30}$$

where v_i and v_j are the velocity vectors, and x_i and x_j are the position vectors.

According to Fig. 10, the density of E increases in the region where the microcavitation is actively generated. The vapor fraction of the microcavitation increases with an increase in the mag-

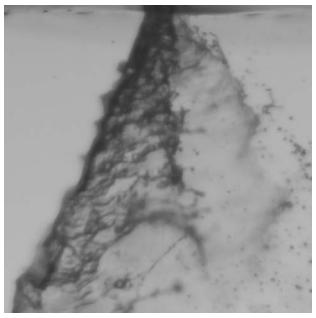

(*a*) Instantaneous photo image

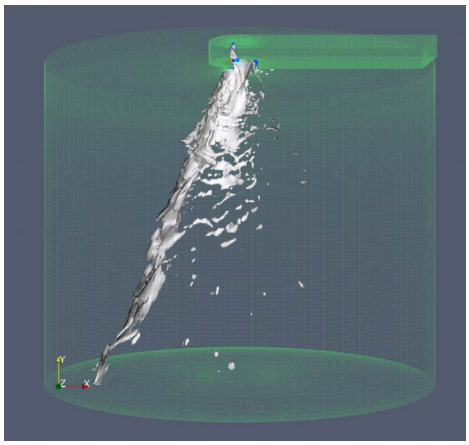

(*b*) Model with cavitation (Case (A))

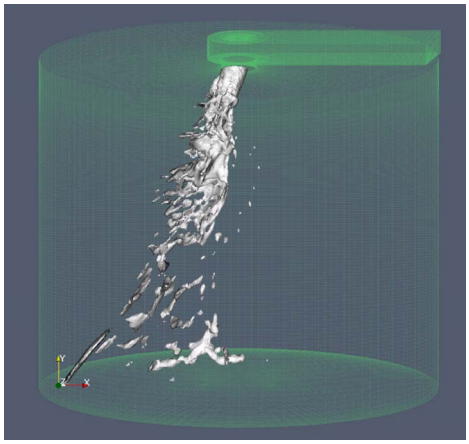

(*c*) Model without cavitation (Case (B))

Fig. 9 Characteristic atomizing spray behavior in comparison with results of models with and without cavitation under primary breakup at a quasi-steady condition (t=8.5×10^{-4} s)

nitude of the vortex. It is also found that the density of E increases in the region where droplet atomization actively occurs and that the energy of vorticity close to the gas-liquid interface is converted to the energy for microcavity generation or droplet atomization. As the velocity in the center of the liquid column is greater than that at the column periphery, the vortices tend to approach the liquid-gas interface. Because enstrophy develops in the downstream region of the aperture, the atomization caused by the separation of the small liquid droplets from the perturbed liquid column with subsequent K-H instability is enhanced by the growth of the amplitude of the wavy liquid film. The perturbation caused by microcavity production also enhances the atomization of small droplets. These greater initial disturbances affecting the jet surface enhance the rapid atomization of droplets, which is closely related to the importance of lateral nozzle-generated turbulence.

According to Fig. 11, especially in the upstream portion of the nozzle aperture where the tornadolike microcavitation is actively generated, vertical eddies are created toward the mainstream. The vertical turbulent vortices are found to be elongated in the vortex-azimuthal direction due to the small-scale swirling flow. It is speculated that the contribution of the turbulent eddy generation is attained by the interference between the microcavities and the shear layer in the small-scale swirling region.

Focusing on the vortex and eddy structures in the primary breakup region where the microcavitation generation-dissipation and the droplet atomization actively occur, the vortices are elongated in the main streamwise direction, which agrees with the direction for enhancement of the breakup of the liquid column. Small eddies are found to be generated in (1) the vicinity of the droplet actively generated region and in its wake region, and (2) the vicinity of the region where microcavitation generation-dissipation actively occurs. In those regions, the magnitude of vorticity has a large value; nevertheless, the size of the eddies are small. Large scale vortices in the entire flow field simulate the internal turbulence, and small scale vortices simulate the microturbulence within the shear layer of microcavities or the boundary layer of the liquid jet flow. The small scale vortices, which have strong vorticity, contribute to the enhancement of atomization. This phenomenon can be explained as resulting from the enhancement of the vertical eddy generation caused by the interference between the droplets and the shear layer in the atomized region, which contributes to the production of turbulent atomization.

Focusing on the effect of microcavitation on the vortex structure, we compared the Q profiles in the case with and that without the cavitation model as shown in Figs. 11 and 12. The diameter of each vertical vortex in the microcavity generated region was found to become smaller than that in the case without the cavitation model. Also the number density of turbulent eddies with the cavitation model was less than that in the case without the cavitation model. These results mean that the energy for the vortex is

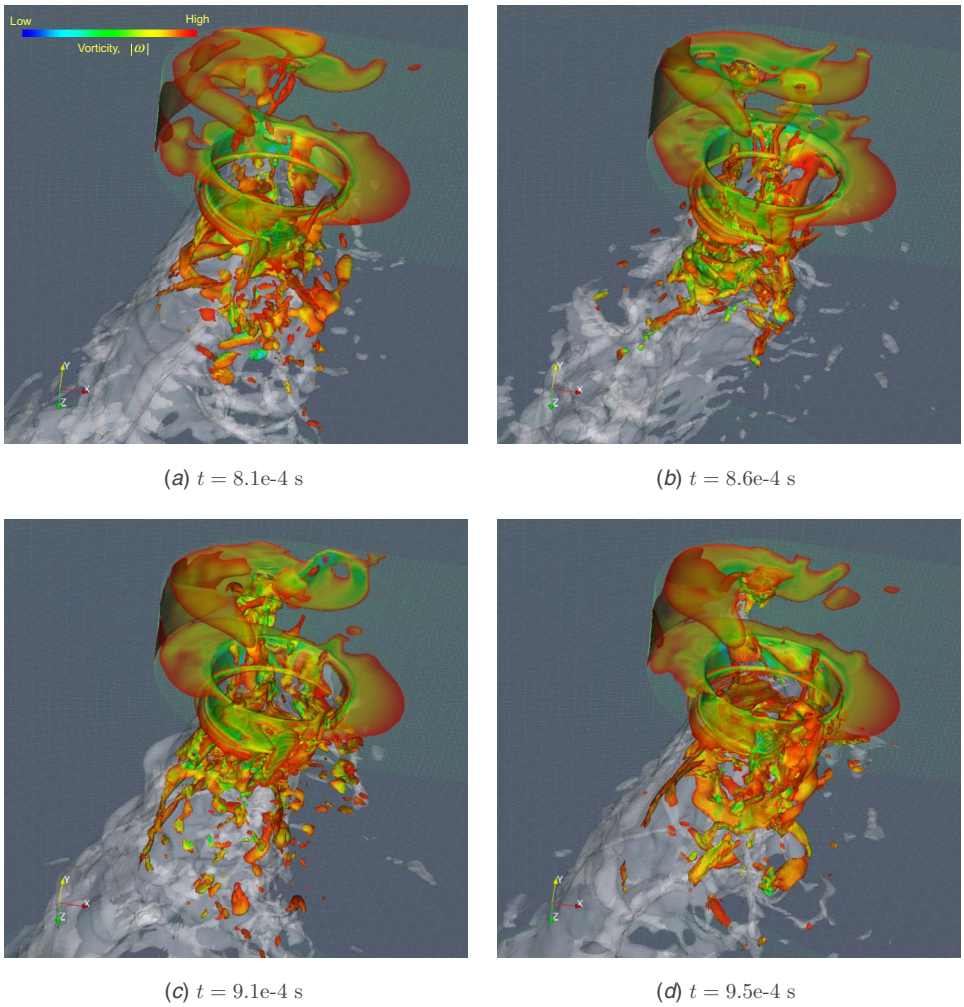

(*a*) $t = 8.1\text{e-}4$ s (*b*) $t = 8.6\text{e-}4$ s

(*c*) $t = 9.1\text{e-}4$ s (*d*) $t = 9.5\text{e-}4$ s

Fig. 10 Instantaneous isosurface of enstrophy *E* profiles just inside and downstream of the nozzle with scalar magnitude of vorticity $|\omega|$

partially converted to the energy for generation of microcavitation. The formation of minute turbulent eddies contributes to the microcavity inception.

Figure 13 shows the statistical result for the frequency of the droplet diameter distribution f_D as a function of streamwise coordinate $-y$ and droplet diameter D_p at integrated time steps under a quasisteady atomizing flow condition.

The statistical method for analyzing the frequency of the droplet diameter profile f_D is described as follows. By dividing the computational domain into about 20 sections in the streamwise direction ($-y$ direction), droplet-size distributions during the statistical time at each cross section can be obtained (See Fig. 14). A rectangular parallelepiped with a certain thin thickness is assumed to be the control section. Namely, f_D denotes the ratio at which a certain droplet diameter occupies the entire droplet diameter distribution. The color graduation denotes the isocontour of the absolute value of f_D.

The frequency f_D was analyzed from the isosurface data of the liquid-vapor volume fraction α, which is given as the threshold of fixed value. When the central point of a certain liquid droplet is located in the internal parallelepiped, this droplet is regarded as a droplet which exists in that cross section. The distribution of the diameter of the atomized droplets is calculated in arbitrary positions in the thin cross-sectional computational region that is perpendicular to the y-axis having a certain thickness. The diameter of each droplet is calculated from droplet volume obtained by taking the volume fraction occupying the computational meshes and the mesh size into account. In the process of diameter profile calculation, the shape of each liquid droplet is assumed to be spherical. If the droplet fraction occupies part of the grid, the ratio of the fractional volume to the grid volume is computed. The droplet fraction is extracted and the equivalent fractional droplet diameter is defined as the diameter of a sphere having the same volume as the fractional droplet, which is regarded as a sphere whose volume is constant (See Fig. 14). This operation enables approximate estimation of the subgrid size fractional droplet diameter. When the droplet diameter profiles are divided equally into n sections, D_p in the nth section is designated as $D_{p(n)}$, and the frequency of the droplet diameter profiles in the range of $D_{p(n-1)}$ to $D_{p(n)}$ in the cross section are obtained at the statistical times under the quasisteady atomizing flow condition [22]. In Fig. 13, the ordinate denotes the droplet diameter distribution frequency f_D, the abscissa denotes the droplet diameter D_p, and the depth directional coordinate denotes the position of the cross section.

It is found that the profile of D_p close to the nozzle aperture region has many discrete peaks, and that the profile exhibits inhomogeneous size distribution; however, with an increase in the streamwise coordinate $(-y)$, the peak frequency of small droplet size appears. Furthermore, the dispersion of droplet-size distribution becomes small and the magnitude of discrete peak frequency

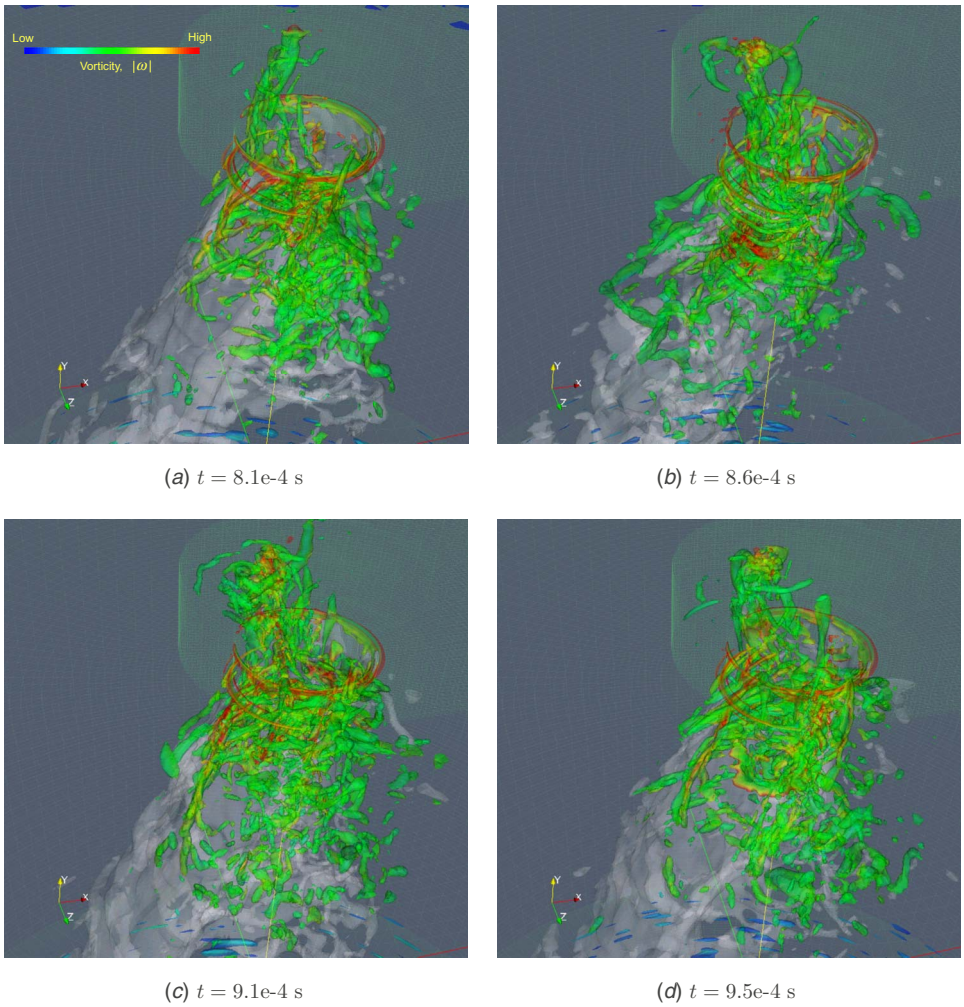

(*a*) $t = 8.1\text{e-}4$ s (*b*) $t = 8.6\text{e-}4$ s

(*c*) $t = 9.1\text{e-}4$ s (*d*) $t = 9.5\text{e-}4$ s

Fig. 11 Instantaneous isosurface of the second invariant of velocity gradient tensor *Q* profiles just inside and downstream of the nozzle with scalar magnitude of vorticity $|\omega|$ (with cavitation model)

becomes smooth. In other words, homogeneous liquid-droplet atomization is gradually enhanced as the cross-sectional region approaches the outlet section. It is speculated that the sequential effect of microcavitation generation and collapse contribute to attainment of homogeneous liquid-droplet atomization in the injector nozzle.

4 Conclusions

It was possible to accurately simulate complex two-phase turbulent atomizing gasoline injector nozzle flow with break-up, coalescence, compressibility effects, and even the interaction between unstable microcavitation and the free surface. The main results obtained can be summarized as follows.

1. Microcavitation was found to be quite locally generated at the edge of the nozzle aperture as well as in the portion where the curvature of the liquid-phase fraction isosurface becomes large. When the liquid film becomes thin due to stretching and the fluid velocity inside the thin liquid-film layer increases prior to turn-off, microcavitation is generated in that portion due to the local pressure drop.
2. The length of the potential core of the lateral atomizing nozzle flow was found to be shorter than that in the general axisymmetric nozzle flow such as that by previous analysis. The short length of the potential core is caused by the strong perturbation due to the orthogonal direction of the inflow duct and the mainstream outflow from the aperture, as well as to microcavity generation. The numerically obtained spray angle characteristic and the tendency of the primary breakup process agree with that of the instantaneous photo image of injector spray by experiment.
3. It was clarified that the density of the enstrophy increases in the region where the microcavitation is actively generated. It was also found that the density of the enstrophy increases in the region where droplet atomization actively occurs. The energy of vorticity close to the gas-liquid interface is converted to energy for microcavity generation or droplet atomization. It was speculated that the contribution of the turbulent eddy generation by the interference between the microcavity and the shear layer in the small-scaled swirling region is attained.
4. The profile of droplet diameter close to the nozzle aperture region was found to have many discrete peaks, and to exhibit inhomogeneous size distribution; however, with an increase in the streamwise coordinate, a peak frequency of small droplet size appears. Namely, homogeneous liquid-droplet atomization is gradually enhanced as the objective region approaches the outlet section. The sequential microcavitation generation and collapse may contribute to attainment of homogeneous liquid-droplet atomization.

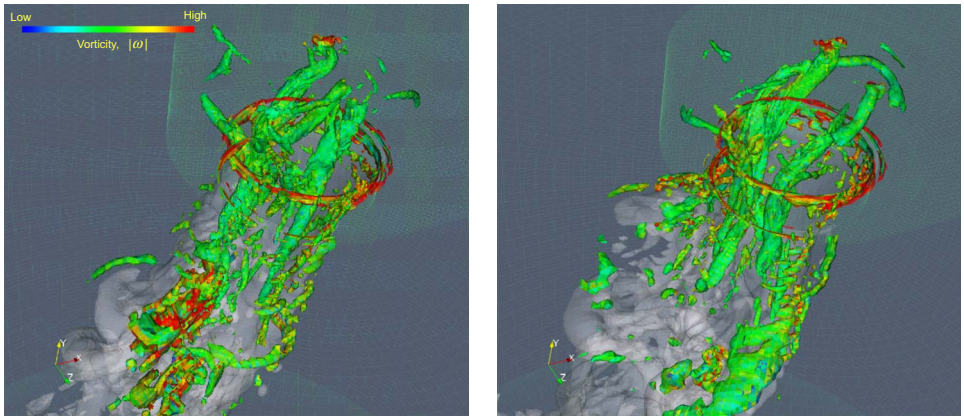

(*a*) $t = 8.1\text{e-}4$ s (*b*) $t = 8.6\text{e-}4$ s

(*c*) $t = 9.1\text{e-}4$ s (*d*) $t = 9.5\text{e-}4$ s

Fig. 12 Instantaneous isosurface of the second invariant of velocity gradient tensor *Q* profiles just inside and downstream of the nozzle with scalar magnitude of vorticity $|\omega|$ (without cavitation model)

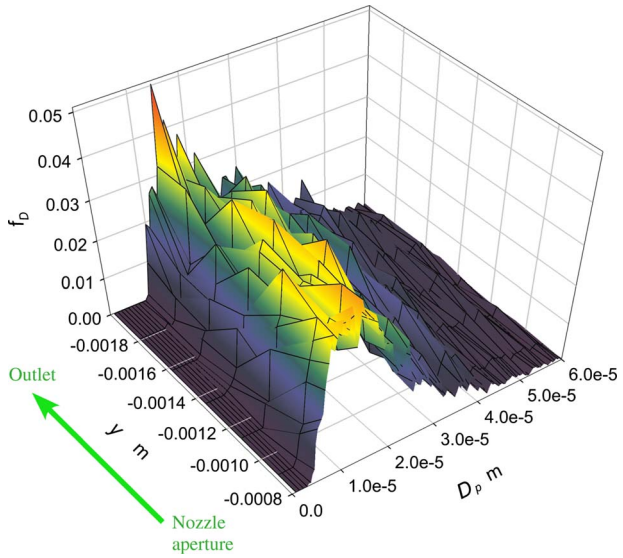

Fig. 13 Statistical result for the frequency of the droplet diameter distribution f_D as a function of streamwise coordinate ($-y$) and droplet diameter D_p at all integrated time steps. The threshold of fixed value α is α=0.1.

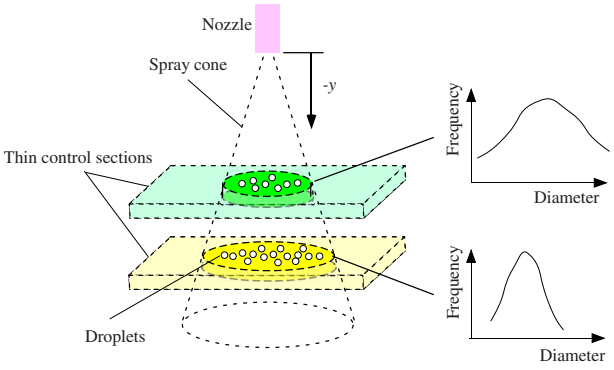

(a) Statistical analysis of droplet diameter profiles

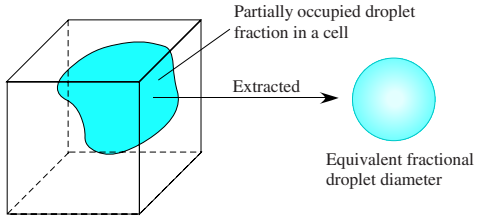

(b) Treatment of subgrid scale size of droplet diameter

Fig. 14 Schematic of the statistical analysis of frequency of droplet diameter profile

Nomenclature

a = sound velocity
D_p = droplet diameter
$\mathrm{D}/\mathrm{D}t$ = substantial derivative
E = enstrophy
f = frequency
k = subgrid-scale turbulent energy
$\boldsymbol{n}$ = unit vector normal
p = absolute pressure
Q = second invariant of velocity gradient tensor
t = time
$\boldsymbol{v}$ = vector of velocity
α = liquid-vapor phase fraction
β = gas-phase fraction $(=1-\alpha)$
γ = cavity (vapor-phase) fraction
ϵ = SGS turbulent dissipation
κ = curvature of the fluid surface
μ = dynamic viscosity
ρ = density
ψ = compressibility
σ = surface tension coefficient
$\boldsymbol{\tau}$ = viscous stress tensor
$\boldsymbol{\omega}$ = vector of vorticity

Subscripts and Superscripts

$()_g$ = gas phase
$()_l$ = liquid phase
$()_{lv}$ = liquid-vapor mixture phase
$()^{\mathrm{sat}}$ = saturation condition
$()_v$ = vapor phase
$()^0$ = initial stationary state

References

[1] Faeth, G. M., Hsiang, L. P., and Wu, P. K., 1995, "Structure and Breakup Properties of Sprays," Int. J. Multiphase Flow, **21**(1), pp. 99–127.
[2] Sallam, K. A., Dai, Z., and Faeth, G. M., 2002, "Liquid Breakup at the Surface of Turbulent Round Liquid Jets in Still Gases," Int. J. Multiphase Flow, **28**(3), pp. 427–449.
[3] Sallam, K. A., Dai, Z., and Faeth, G. M., 1999, "Drop Formation at the Surface of Plane Turbulent Liquid Jets in Still Gases," Int. J. Multiphase Flow, **25**, pp. 1161–1180.
[4] Lin, S. P., 2003, *Breakup of Liquid Sheets and Jets*, Cambridge University Press, New York.
[5] Lin, S. P., and Reitz, R. D., 1998, "Drop and Spray Formation From a Liquid Jet," Annu. Rev. Fluid Mech., **30**, pp. 85–105.
[6] Zaleski, S., Li, J., and Succi, S., 1995, "Two-Dimensional Navier-Stokes Simulation of Deformation and Breakup Of Liquid Patches," Phys. Rev. Lett., **75**(2), pp. 244–247.
[7] Leboissetier, A., and Zaleski, S., 2001, "Direct Numerical Simulation of the Atomization of Liquid Jet," Proceeding of the ILASS-Europe 2001, Zurich, Sep. 2–6.
[8] Villiers, D. E., 2004, "The Potential of Large Eddy Simulation for the Modeling of Wall Bounded Flows," Ph.D. thesis, Imperial College of Science, Technology and Medicine, London, UK.
[9] Schmidt, D. P., Rutland, C. J., and Corradini, M. L., 1999, "A Fully Compressible Model of Small, High Speed, Cavitating Nozzle Flows," Atomization Sprays, **9**, pp. 255–276.
[10] von Berg, E., Edelbauer, W., Alajbegovic, A., Tatschl, R., Volmajer, M., Kegl, B., and Ganippa, L. C., 2005, "Coupled Simulations of Nozzle Flow, Primary Fuel Jet Breakup, and Spray Formation," Trans. ASME J. Eng. Gas Turbines Power, **127**(4), pp. 897–908.
[11] Yuan, W., and Schnerr, G. H., 2003, "Numerical Simulation of Two-Phase Flow in Injection Nozzles: Interaction of Cavitation and External Jet Formation," Trans. ASME J. Fluids Eng., **125**(6), pp. 963–969.
[12] OpenCFD, 2009, http://www.opencfd.co.uk/.
[13] Apte, S. V., Gorokhovski, M., and Moin, P., 2003, "LES of Atomizing Spray With Stochastic Modeling of Secondary Breakup," Int. J. Multiphase Flow, **29**(9), pp. 1503–1522.
[14] Vinkovic, I., Aguirre, C., Simoëns, S., and Gorokhovski, M., 2006, "Large Eddy Simulation of Droplet Dispersion for Inhomogeneous Turbulent Wall Flow," Int. J. Multiphase Flow, **32**(3), pp. 344–364.
[15] Hirt, C. W., and Nichols, B. D., 1981, "Volume of Fluid (VOF) Method for the Dynamics of Free Boundaries," J. Comput. Phys., **39**(1), pp. 201–225.
[16] Garbero, M., Vanni, M., and Fritsching, U., 2006, "Gas/Surface Heat Transfer in Spray Deposition Processes," Int. J. Heat Fluid Flow, **27**(1), pp. 105–122.
[17] Puckett, E. G., Almgren, A. S., Bell, J. B., Marcus, D. L., and Rider, W. J., 1997, "A High-Order Projection Method for Tracking Fluid Interfaces in Variable Density Incompressible Flows," J. Comput. Phys., **130**(2), pp. 269–282.
[18] Brackbill, J. U., Kothe, D. B., and Zemach, C., 1992, "A Continuum Method for Modeling Surface Tension," J. Comput. Phys., **100**, pp. 335–354.
[19] Weller, H. G., and Tabora, G., 1998, "A Tensorial Approach to Computational Continuum Mechanics Using Object-Oriented Techniques," Comput. Phys., **12**(6), pp. 620–631.
[20] Ubbink, O., and Issa, R. I., 1999, "A Method for Capturing Sharp Fluid Interfaces on Arbitrary Meshes," J. Comput. Phys., **153**, pp. 26–50.
[21] Leonard, B. P., 1991, "A Stable and Accurate Convection Modelling Procedure Based on Quadratic Upstream Interpolation," Comput. Methods Appl. Mech. Eng., **88**(1), pp. 17–74.
[22] Ishimoto, J., Ohira, K., Okabayashi, K., and Chitose, K., 2008, "Integrated Simulation of the Atomization Process of a Liquid Hydrogen Jet Through a Cylindrical Nozzle," Cryogenics, **48**(5–6), pp. 238–247.